

# Computational exploration of a viable route to the Kitaev-quantum spin liquid phase in monolayer OsCl<sub>3</sub>

Qiangqiang Gu,<sup>1,2</sup> Shishir Kumar Pandey,<sup>2,\*</sup> and Yihao Lin<sup>3</sup>

<sup>1</sup>*School of Mathematical Science, Peking University, Beijing 100871, China*

<sup>2</sup>*AI for Science Institute, Beijing, China*

<sup>3</sup>*International Center for Quantum Materials, School of Physics, Peking University, Beijing 100871, China*

(Dated: June 6, 2023)

In this computational study, we explore a viable route to access the Kitaev-Quantum Spin Liquid (QSL) state in recently synthesized monolayer of a so-called spin-orbit assisted Mott insulator OsCl<sub>3</sub>. In addition to other magnetic ground states in different regions, the small  $J_H/U$  region of our Hubbard  $U$ -Hund's  $J_H$  quantum phase diagram, obtained by combining second-order perturbation and pseudo-Fermion renormalization group calculations, hosts Kitaev-QSL phase. Only Kitaev interaction of a smaller magnitude is obtained in this region. Negligibly small farther neighbor interactions appear as a distinct feature of monolayer OsCl<sub>3</sub>, suggesting this material to be a better candidate for the exploration of possible Kitaev-QSL state than earlier proposed materials. Insights from our study might be useful to probe magnetic phase transitions by purportedly manipulating  $U$  and  $J_H$  with epitaxial strain in advanced crystal growth techniques.

The Kitaev honeycomb model with bond-dependent Ising-type exchange interactions on a honeycomb lattice naturally hosts the novel quantum spin liquid (QSL) state<sup>1</sup>. The realization of the Kitaev model in so-called spin-orbit coupling (SOC) assisted Mott insulators was proposed by Jackeli and Khaliullin<sup>2</sup>. This requires SOC active transition-metal ions to be in edge-shared octahedral crystal field (CF) of anions, and Sr<sub>2</sub>IrO<sub>4</sub> was initially proposed as an example<sup>2</sup>. Since then, many materials like  $\alpha$ -RuCl<sub>3</sub><sup>3-7</sup> and Cobaltates<sup>8-17</sup>, other Iridates<sup>18-25</sup> are proposed as pertinent Kitaev-QSL candidates<sup>26,27</sup>. In these materials, the formation of  $j_{\text{eff}} = 1/2$  Kramers doublets, which form the low-energy space in the materials, results from the interplay of octahedral CF ( $\Delta^{\text{CF}}$ ) and SOC.

Although the dominant magnetic interaction between these pseudospin 1/2 states is proposed to be Kitaev ( $K$ ) type<sup>2</sup>, other *undesirable* interactions such as isotropic Heisenberg ( $J$ ) and off-diagonal terms ( $\Gamma$ ), as well as farther neighbor couplings, also appear, causing long-range magnetic order in the materials mentioned above, and driving them away from a possible QSL ground state. For example, the appearance of third nearest neighbor (3NN)  $J_3$ <sup>28</sup> and strong neutron absorbing Ir ions along with rapidly decaying magnetic form factor with an increase in momentum transfer in inelastic neutron scattering experiments on Iridates are some of the experimental challenges<sup>21,27</sup>. In another example, smaller SOC strength of Ru<sup>+3</sup> ions as well as a significant  $J_3$  in  $\alpha$ -RuCl<sub>3</sub> are the hurdles in the quest of QSL state in this material. Despite such inevitable challenges, attempts have been made to access the QSL state using external knobs. For example, magnetic interactions in  $\alpha$ -RuCl<sub>3</sub> were manipulated by means of the external magnetic field to achieve the QSL state<sup>29-31</sup>. In another theoretical attempt by Liu *et. al.*<sup>11</sup>,  $\Delta_{\text{tri}}^{\text{CF}}$  was proposed as a tunable parameter with pressure to realize QSL state in Cobaltates. Towards this goal, our computational study in this article aims to

explore the Kitaev-QSL state in SOC-assisted Mott insulators through manipulation of the fundamental electronic parameters  $U$  and  $J_H$ . Our study is also motivated in part by recent theoretical work that argues for the experimental tuning of  $U$  and  $J_H$  parameters in perovskites with epitaxial strain, based on advancements in experimental epitaxial growth techniques<sup>32</sup>.

To realize our goal, we consider the OsCl<sub>3</sub> monolayer as a case study. Our material choice is based on the fact it satisfies all the necessary criteria mentioned earlier to host strong Kitaev interactions, *viz* Os<sup>+3</sup> 5d<sup>5</sup> ions in the edge-shared OsCl<sub>6</sub> octahedron possess large SOC interaction. In a recent experimental study by Kataoka *et. al.*<sup>33</sup>, magnetization and heat capacity measurements on Os<sub>0.81</sub>Cl<sub>3</sub> revealed the absence of any long-range magnetic ordering of Os<sup>+3</sup> spins arranged on the triangular lattice (with local honeycomb domain formation) up to 0.08 K temperature, which can be an indication of underlying strong magnetic frustration in this compound, also a building block for Kitaev physics. A previous computational attempt to study the topological properties of this compound proposed a ferromagnetic (FM) ground state for the monolayer OsCl<sub>3</sub><sup>34</sup>, but a scrupulous investigation of its magnetic properties is warranted in the light of the fact that the iso-electronic  $\alpha$ -RuCl<sub>3</sub> has a zigzag (ZZ) antiferromagnetic (AFM) ground state. From a computational modeling perspective, electronic parameters  $U$  and  $J_H$  are part of Hubbard-Kanamori  $H_{\text{int}}$  Hamiltonian in Eq. S4. The full model Hamiltonian  $\mathcal{H}$  in Eq. S4 has been quite successful and hence, widely accepted for the estimation of magnetic interactions in these materials<sup>7,16,28,35,36</sup>. Thus, one can explore the access to the Kitaev-QSL phase by tuning the  $U$  and  $J_H$  parameters and calculating the corresponding magnetic interactions which is the objective of this article.

We first used *ab initio* calculations of higher accuracy to show that the ZZ and FM configurations in this material are nearly degenerate, indicating highly compet-

ing magnetic interactions that may be a reason for the absence of long-range magnetic ordering in this compound. We then varied  $U$  and  $J_H/U$  in the second-order perturbation calculations to obtain magnetic interactions and input them into pseudofermion functional renormalization-group (pf-FRG) calculations, which allowed us to obtain a  $U$ - $J_H/U$  quantum phase diagram. At small values of  $J_H/U$ , we found the emergence of only  $K$ -type 1NN interaction, albeit of smaller magnitude, resulting in the Kitaev-QSL state occupying a substantial part of the phase diagram. In addition to the QSL state, we also find FM, ZZ, and Néel states present in different parts of the phase diagram. Much more advantageous than previously suggested Kitaev-QSL material candidates like Iridates,  $\alpha$ - $\text{RuCl}_3$  and Cobaltates, we find that the second and third neighbor magnetic interactions are negligibly smaller in the monolayer  $\text{OsCl}_3$ , suggesting this material to be a better candidate for the exploration of possible Kitaev-QSL state.

*Crystal structure and magnetism – ab initio calculations:* We consider the  $C2/m$  honeycomb crystal structure of the monolayer  $\text{OsCl}_3$  which is similar to  $\alpha$ - $\text{RuCl}_3$ <sup>34,37</sup>. Very recently, a triangular lattice with nanometer-sized honeycomb domains of Os atoms has been observed experimentally<sup>33</sup>. The structure is shown in Fig. 1(a) and Fig. S1 of supplementary material (SM)<sup>38</sup>. The full optimization of lattice constants within highly accurate *ab initio* calculations after imposition of both ZZ and FM state brings nearly identical crystal structure in both cases. Our phonon calculations with this optimized crystal structure indicate that the honeycomb lattice of  $\text{OsCl}_3$  monolayer is at least dynamically stable. Details of *ab initio* calculations, optimized crystal structure, and phonon calculations can be found in Sec. S1 of SM<sup>38</sup>.

To understand the nature of magnetism and underlying frustration, highly accurate *ab initio* total energy calculations are performed, with tighter energy and force convergence criterion, after imposing various magnetic configurations like FM, ZZ, Néel, and Stripe. We varied  $U$  on Os  $d$  states in the range 0.1–3 eV and the SOC effect is self-consistently included. The results, shown in Fig. 1(b) reveal that the ZZ state is lowest in energy when the spins are canted in an out-of-plane direction towards the center of one of the Cl-Cl edges in an  $\text{OsCl}_6$  octahedron (see Fig. 1(a)), with the closely competing FM state higher in energy. Other AFM configurations like Néel and stripe are energetically much higher. Such orientation of magnetic moments was also proposed for  $\text{Na}_2\text{IrO}_3$ <sup>39,40</sup>. The energy difference between the ZZ and FM state nearly vanishes for the in-plane arrangement of spins along the  $a$  axis as shown in Fig. 1(d). This is consistent with the previous study by Sheng *et al.*<sup>34</sup>. The nearly degenerate FM and ZZ configurations, which differ by a single 1NN spin flip, are indicative of large magnetic frustration present in the system, explaining the absence of long-range magnetic ordering observed in experiment<sup>33</sup>. The larger energy difference between other AFM

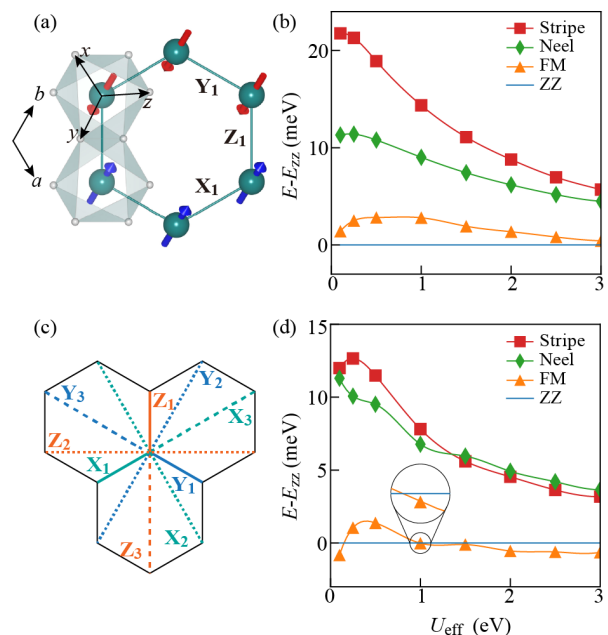


FIG. 1. (a) Top view of out-of-plane spin arrangement on a hexagon in ZZ magnetic state in monolayer  $\text{OsCl}_3$ . Spins point towards the center of one of the Cl-Cl edges in an  $\text{OsCl}_6$  octahedron. Big Cyan and small gray balls represent Os and Cl atoms;  $x$ ,  $y$  and  $z$  are local axes while  $a$  and  $b$  are crystallographic axes. Variation of the total energy of different magnetic configurations relative to ZZ state with  $U$  on Os  $d$  states for, (b) out-of-plane spin alignment, and (d) alignment of spins along  $a$  axis. (c) Color-coded X, Y, and Z bonds up to 3NN are shown.

states, like Néel and stripe, and ZZ state may indicate that the exchange interactions in monolayer  $\text{OsCl}_3$  may not be weak. In the most simplistic second-order perturbation theory, magnetic exchange interactions are  $\propto t^2/U$  at large  $U$  values if one treats hopping  $t$  as a perturbation. The expected  $1/U$  behavior<sup>41,42</sup> of magnetic stability curves in Fig. 1 (b) and (d) at large values  $U$  is apparent. We also find that the in-plane magnetic anisotropy for monolayer  $\text{OsCl}_3$  is quite small (see Fig. S3 of SM<sup>38</sup>). Next, we describe the electronic Hamiltonian considered in this study for exploration of  $U$ - $J_H$  quantum phase diagram in the quest of QSL state.

*Model Hamiltonian:* The full Hamiltonian for  $d^5$  systems is given as<sup>7,16,28,35</sup>,

$$\mathcal{H} = H_{\text{hop}} + H_{\text{cf}} + H_{\text{soc}} + H_{\text{int}} \quad (1)$$

where terms on the right-hand side are hopping, CF, SOC, and Hubbard-Kanamori Hamiltonians, respectively. For Mott insulators, in limit  $t \ll U$ , one can separate the “onsite” term  $H_i^0$  from  $\mathcal{H}$ .  $H_i^0$ , represented in basis  $\psi_{i\sigma}^\dagger = [d_{z^2}^\dagger, d_{xz}^\dagger, d_{yz}^\dagger, d_{x^2-y^2}^\dagger, d_{xy}^\dagger]_{i\sigma}$  for site  $i$  and

spin  $\sigma$ , then reads as,

$$\begin{aligned}
H_i^0 &= H_{\text{cf}} + H_{\text{soc}} + H_{\text{int}} \\
&= \sum_{\sigma} \psi_{i\sigma}^{\dagger} \Delta_i^{\text{CF}} \psi_{i\sigma} + \sum \lambda \mathbf{L}_i \cdot \mathbf{s}_i \\
&+ \frac{U}{2} \sum_{\alpha} n_{i\alpha\sigma} n_{i\alpha\sigma'} + \frac{U'}{2} \sum_{\alpha \neq \beta} n_{i\alpha} n_{i\beta} \\
&- \frac{J_{\text{H}}}{2} \sum_{\sigma, \sigma', \alpha \neq \beta} \psi_{i\alpha\sigma}^{\dagger} \psi_{i\alpha\sigma'} \psi_{i\beta\sigma'}^{\dagger} \psi_{i\beta\sigma} \\
&- \frac{J'}{2} \sum_{\sigma \neq \sigma', \alpha \neq \beta} \psi_{i\alpha\sigma}^{\dagger} \psi_{i\beta\sigma'} \psi_{i\alpha\sigma'}^{\dagger} \psi_{i\beta\sigma} \quad (2)
\end{aligned}$$

In above expression,  $U/U'$  are intraorbital/interorbital Coulomb interaction terms, and  $J_{\text{H}}$  and  $J'$  are Hund's coupling and pair hopping interaction, respectively.  $U' = U - 2J_{\text{H}}$  and  $J_{\text{H}} = J'$  is considered in the above equation. To bring complete rotational invariance of  $H_i^0$  in the presence of  $e_g$  orbitals, the inclusion of additional three and four orbitals terms in  $H_{\text{int}}$  should be considered. However, for large  $\Delta_i^{\text{CF}}$ , such additional terms have an imperceptible influence on magnetic interactions. A discussion around this point is included in Sec. 4(a) of SM<sup>38</sup>.  $\Delta_i^{\text{CF}}$  and hopping amplitudes  $t_{ij}$  in  $H_{\text{hop}} = \sum_{i \neq j, \sigma} \psi_{i\sigma}^{\dagger} T_{ij} \psi_{j\sigma}$  are obtained from a Wannier based tight-binding (TB) model excluding SOC effect. The strength of SOC in monolayer OsCl<sub>3</sub>,  $\lambda = 0.355$  eV, is estimated by a band-structure fitting procedure (see Sec S2<sup>38</sup> for details). As proposed earlier, it might be possible to experimentally tune parameters  $U$  and  $J_{\text{H}}$  by epitaxial strain in advance growth techniques<sup>32</sup>. Hence, we vary these two parameters to explore the possibility of QSL state in monolayer OsCl<sub>3</sub>. For a  $d^5$  system, the dimension of Hilbert spaces for  $H_i^0$  is  $C_5^{10} = 252$  and by exactly diagonalizing it, we obtain the lowest two eigenstates as the  $j_{\text{eff}} = 1/2$  Kramers doublet. We then use the second-order perturbation method, treating hopping as a perturbation, to estimate magnetic interactions between these pseudo-spin states. Details of the methodology and discussions on the validity of low-energy  $j_{\text{eff}} = 1/2$  picture and atomic features which can be observed in experiments for monolayer OsCl<sub>3</sub> are presented in Sec. S3, S4 and S6 of SM<sup>38</sup>.

*Magnetic interactions and quantum phase diagram:* Estimated magnetic interactions up to 3NN (Fig. 1(c) depicts bonds up to 3NN) from second-order perturbation method are used as input for the pf-FRG calculations. We then analyzed the ground states by plotting the static spin correlation function, obtained from pf-FRG calculations, in the first and extended BZ of monolayer OsCl<sub>3</sub>. Our choice of the pf-FRG method as a quantum toolkit is based on its earlier demonstrated success in exploring quantum phase diagrams on different lattice and spin models<sup>43,44</sup>. Our obtained quantum phase diagram for a range of  $U$  (0.5 - 3.0 eV) and  $J_{\text{H}}/U$  (0.075 - 0.3) is shown in Fig. 2(a). This range of parameters is chosen so that the phase space is extended on either side of the point  $U = 1.7$  eV and  $J_{\text{H}} = 0.3$  eV ( $J_{\text{H}}/U \sim 0.176$ ) pre-

viously considered for 5d system such as Iridates in the literature<sup>28</sup>. Details of pf-FRG calculations are given in Sec. S5 of SM<sup>38</sup>. We will now discuss this phase diagram in detail.

TABLE I. Estimated bond-dependent magnetic interactions for monolayer OsCl<sub>3</sub> using second-order perturbation method at  $U = 1.7$  eV,  $J_{\text{H}} = 0.3$  eV and  $\lambda = 0.355$  eV. Values of Heisenberg  $J$ , Kitaev  $K$ , off-diagonal  $\Gamma$ ,  $\Gamma'$  and asymmetric DMI  $\mathbf{D}$  terms along with diagonal and off-diagonal anisotropic terms  $\xi$  and  $\zeta$  are listed. 3NN interactions as well as some 2NN interactions are  $< 0.05$  meV and hence not listed here.

Magnetic interactions (meV)						
Bond	$J$	$K$	$\Gamma$	$\Gamma'$	$\xi$	$\zeta$
X <sub>1</sub>	-1.055	-14.600	5.662	-3.578	0.520	2.515
Y <sub>1</sub>	-0.961	-17.215	6.010	-0.748	-0.213	-4.320
Z <sub>1</sub>	-0.844	-15.127	4.749	-2.342	-1.285	-4.567
X <sub>2</sub>	-0.294	0.533	0.206	-0.197	-	-0.082
Y <sub>2</sub>	0.145	0.878	0.050	-0.150	-	-0.167
Z <sub>2</sub>	-0.258	0.453	0.086	-0.246	-	-0.050
$\mathbf{D}_{ij}$						
X <sub>2</sub>	( 0, 0, 0)					
Y <sub>2</sub>	(-0.350, 0, -0.216)					
Z <sub>2</sub>	(-0.108, -0.125, 0)					

Various magnetic phases *viz* FM, ZZ and Néel and QSL states occupy different parts of the phase diagram. At smaller values of  $U = 0.5$  eV and  $J_{\text{H}}/U = 0.075 - 0.15$ , there is a ( $< 1.5$  meV) 1NN FM  $J$  which is slightly larger than the AFM  $K$  coupling resulting in an FM ground state with a competing ZZ phase. This behavior manifested in a star-like shape of static spin susceptibility (hereafter only susceptibility) plot in Fig. 2(c) (last plot). Consistent with the FM phase, the major contribution to the susceptibility comes from the zone center while small spreads along  $M$ -points in the first BZ indicate a competing ZZ AFM phase. Transition to later happens when both couplings change their respective signs with FM  $K >$  AFM  $J$ , which is consistency with a recent observation on Cobaltates<sup>16</sup>. At a typical phase point  $U = 0.5$  eV and  $J_{\text{H}}/U = 0.1$  in this region, depicted by white star in Fig. 2(a), we obtained  $J = -0.5$  meV  $K = 0.35$  meV.

In ZZ region, away from the FM-ZZ phase boundary, other terms like  $\Gamma$ ,  $\Gamma'$ ,  $\xi$ ,  $\zeta$  as well as smaller farther neighbor interactions started to emerge in the ZZ region of the phase diagram. However, 1NN dominant  $K$  and  $J$  terms remain FM and AFM, respectively. We emphasize here that 2NN and 3NN interactions are at least 2 ~ 3 orders of magnitude smaller than 1NN and have no qualitative effect on the magnetic ground state. Values of  $U = 1.7$  eV and  $J_{\text{H}} = 0.3$  eV bring ZZ state (white star in ZZ region in Fig. 2(a)) and estimated interactions are listed in Table I. The corresponding susceptibility plot in Fig. 2(c) (second from the left) has dominant contributions from  $M$ -points of the first BZ, consistent with the underlying ZZ magnetic order. In the absence of inversion symmetry

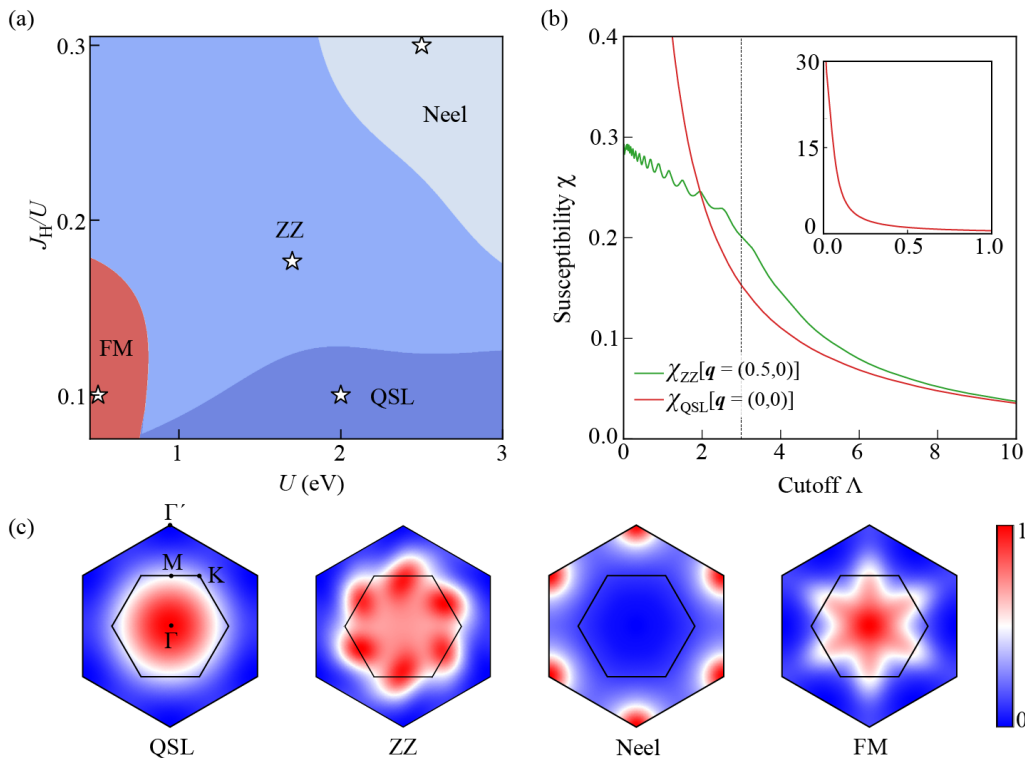


FIG. 2. (a) Magnetic quantum phase diagram in  $U$ - $J_H/U$  parameter space obtained using a combination of second-order perturbation and pf-FRG calculations. The range considered is  $U = 0.5 - 3.0$  eV and  $J_H/U = 0.075 - 0.3$  are considered. Obtained magnetic phases are FM, ZZ, Néel, and QSL magnetic states. Static spin correlation plots in (c) correspond to the points depicted by star symbols in (a). Intensity is normalized for each plot in (c), and the inner and outer hexagons in these plots denote the first and extended BZ of monolayer OsCl<sub>3</sub>. (b) The renormalization group flow of the magnetic correlations ( $\chi$ ) for the two cases, ZZ (green curve) and QSL (red) states with an inset showing the flow at low frequencies for the QSL state. Vertical dash lines show the break of the flow of  $\chi$  for the ZZ state while its smooth flow for the QSL state is indicative of no spontaneous symmetry breaking.

on the 2NN bonds, a small Dzyaloshinskii–Moriya interaction (DMI) appears for these magnetic neighbors. We would like to mention that the value of  $U$  and  $J_H$  obtained from cRPA calculations also brings a ZZ state, details of which are provided in Sec. S7 of SM<sup>38</sup>. ZZ phase occupying the largest part of the phase diagram quantitatively differs in different regions and a related discussion is provided in Sec. S7 of SM<sup>38</sup>. Further increase of  $U$  ( $\approx 2 - 3$  eV) and  $J_H/U$  ( $\approx 0.2 - 0.3$ ) stabilizes Néel AFM state, with 1NN AFM  $J$  being the dominant interaction while all other interactions are highly suppressed. For a typical phase point  $U = 2.5$  eV,  $J_H/U = 0.3$  (marked by a white star in Néel region), 1NN, 2NN, and 3NN  $J$  values are 3.39, 0.39 and 0.03 meV, respectively. Contribution from  $\Gamma'$  points of the extended BZ in the corresponding susceptibility plot shown in Fig. 2(c) (third from the left) is consistent with the underlying Néel magnetic order.

Most importantly, a substantial region of the phase diagram, in the range of  $U = 1.0 - 3.0$  eV,  $J_H/U = 0.075 - 0.1$ , is occupied by the Kitaev-QSL state. In this region, we only obtained a small but finite 1NN FM  $K$  term ( $\sim 1$  meV) in our second-order perturbation calculations. The susceptibility plot for this state shown in Fig. 2(c)

(leftmost) has a contribution from the whole first BZ, with the highest intensity appearing at the  $\Gamma$  point. No long-range magnetic ordering and hence, no spontaneous symmetry breaking is expected for this state even at low temperatures. To verify this, we can plot the renormalization group flow of the magnetic correlations ( $\chi$ ) as a function of the renormalization group cutoff ( $\Lambda$ ). Spontaneous symmetry breaking by the onset of a long-range magnetic ordering at a  $\Lambda$  results in a kink or break of  $\chi$ . The smooth evolution of  $\chi$  down to the lowest  $\Lambda$  can be seen for the QSL state from the red curve in Fig. 2(b) (see also the inset). For comparison, we also show a similar plot for the ZZ order (green curve) corresponding to interactions listed in Table I. Clearly,  $\chi$ , in this case, displays a breakdown at  $\Lambda_c \approx 3.3$  signaling the onset of the ZZ order.

Several remarks are in order. First, though off-diagonal magnetic coupling (e.g.  $\Gamma$ ) is large compared to Iridates<sup>28</sup>, orders of magnitude smaller farther neighbor magnetic interactions (3NN interactions are all  $< |0.05|$ ) distinguishes monolayer OsCl<sub>3</sub> these earlier proposed Kitaev-QSL candidates including Iridates<sup>16,28</sup>. Second, strain as an external knob, proposed in Ref.<sup>32</sup> for tuning



$U$  and  $J_H$  can also be utilized to tune trigonal distortions as suggested in Ref.<sup>11</sup>. The strain in this case can also alter the hopping amplitudes between  $d$  orbitals. Hence, it would be interesting to probe the role of strain in tuning the magnetic properties of these QSL candidate materials. Third, tuning of  $U$  and  $J_H$  to access the QSL region in the phase diagram can also be achieved through the choice of suitable elements from the periodic table. Advancement in material synthesis techniques can be of great help here.

In conclusion, considering recently synthesized monolayer  $\text{OsCl}_3$  as an example, we have explored a route to access Kitaev QSL state by varying electronic parameters Hubbard  $U$  and Hund's  $J_H$ . These two parameters purportedly can be tuned experimentally with epitaxial strain. Using highly accurate *ab initio* total energy calculations, we have shown that the ZZ and FM are nearly degenerate indicating the large magnetic frustration which might be the possible reason behind the absence of long-range magnetic ordering in this material.

Combining second-order perturbation and pf-FRG calculations, we presented a magnetic quantum phase diagram in  $U$ - $J_H/U$  space. A substantial part of this phase diagram hosts the Kitaev QSL state, stabilized by 1NN Kitaev interaction only, with other magnetic phases like FM, ZZ, and Néel AFM states also appearing in different regions of the phase diagram stabilized by changing dominant magnetic interactions. Insights obtained from our study may be helpful in designing experiments on pertinent Kitaev-QSL candidate materials.

## ACKNOWLEDGMENTS

QG and SKP contributed equally to this work. SKP gratefully acknowledges valuable feedback from Prof. D. D. Sarma. SKP also acknowledges the careful reading of the manuscript and correspondence on magnetic exchange couplings with Ramesh Dhakal and Dr. Stephen M. Winter.

- 
- \* [shishir.kr.pandey@gmail.com](mailto:shishir.kr.pandey@gmail.com)
- <sup>1</sup> A. Kitaev, Anyons in an exactly solved model and beyond, *Ann. Phys.* **321**, 2 (2006), january Special Issue.
  - <sup>2</sup> G. Jackeli and G. Khaliullin, Mott Insulators in the Strong Spin-Orbit Coupling Limit: From Heisenberg to a Quantum Compass and Kitaev Models, *Phys. Rev. Lett.* **102**, 017205 (2009).
  - <sup>3</sup> K. W. Plumb, J. P. Clancy, L. J. Sandilands, V. V. Shankar, Y. F. Hu, K. S. Burch, H.-Y. Kee, and Y.-J. Kim,  $\alpha$ - $\text{RuCl}_3$ : A spin-orbit assisted Mott insulator on a honeycomb lattice, *Phys. Rev. B* **90**, 041112 (2014).
  - <sup>4</sup> R. D. Johnson, S. C. Williams, A. A. Haghighirad, J. Singleton, V. Zapf, P. Manuel, I. I. Mazin, Y. Li, H. O. Jeschke, R. Valentí, and R. Coldea, Monoclinic crystal structure of  $\alpha$ - $\text{RuCl}_3$  and the zigzag antiferromagnetic ground state, *Phys. Rev. B* **92**, 235119 (2015).
  - <sup>5</sup> A. Banerjee, C. A. Bridges, J.-Q. Yan, A. A. Aczel, L. Li, M. B. Stone, G. E. Granroth, M. D. Lumsden, Y. Yiu, J. Knolle, S. Bhattacharjee, D. L. Kovrizhin, R. Moessner, D. A. Tennant, D. G. Mandrus, and S. E. Nagler, Proximate Kitaev quantum spin liquid behaviour in a honeycomb magnet, *Nat. Mat.* **15**, 733 (2016).
  - <sup>6</sup> H.-S. Kim, V. S. V., A. Catuneanu, and H.-Y. Kee, Kitaev magnetism in honeycomb  $\text{RuCl}_3$  with intermediate spin-orbit coupling, *Phys. Rev. B* **91**, 241110 (2015).
  - <sup>7</sup> W. Wang, Z.-Y. Dong, S.-L. Yu, and J.-X. Li, Theoretical investigation of magnetic dynamics in  $\alpha$ - $\text{RuCl}_3$ , *Phys. Rev. B* **96**, 115103 (2017).
  - <sup>8</sup> H. Liu and G. Khaliullin, Pseudospin exchange interactions in  $d^7$  cobalt compounds: Possible realization of the Kitaev model, *Phys. Rev. B* **97**, 014407 (2018).
  - <sup>9</sup> R. Sano, Y. Kato, and Y. Motome, Kitaev-Heisenberg Hamiltonian for high-spin  $d^7$  Mott insulators, *Phys. Rev. B* **97**, 014408 (2018).
  - <sup>10</sup> M. Songvilay, J. Robert, S. Petit, J. A. Rodriguez-Rivera, W. D. Ratcliff, F. Damay, V. Balédent, M. Jiménez-Ruiz, P. Lejay, E. Pachoud, A. Hadj-Azzem, V. Simonet, and C. Stock, Kitaev interactions in the Co honeycomb antiferromagnets  $\text{Na}_3\text{Co}_2\text{SbO}_6$  and  $\text{Na}_2\text{Co}_2\text{TeO}_6$ , *Phys. Rev. B* **102**, 224429 (2020).
  - <sup>11</sup> H. Liu, J. c. v. Chaloupka, and G. Khaliullin, Kitaev Spin Liquid in  $3d$  Transition Metal Compounds, *Phys. Rev. Lett.* **125**, 047201 (2020).
  - <sup>12</sup> L. Viciu, Q. Huang, E. Morosan, H. Zandbergen, N. Greenbaum, T. McQueen, and R. Cava, Structure and basic magnetic properties of the honeycomb lattice compounds  $\text{Na}_2\text{Co}_2\text{TeO}_6$  and  $\text{Na}_3\text{Co}_2\text{SbO}_6$ , *J. Solid State Chem.* **180**, 1060 (2007).
  - <sup>13</sup> G. Xiao, Z. Xia, W. Zhang, X. Yue, S. Huang, X. Zhang, F. Yang, Y. Song, M. Wei, H. Deng, and D. Jiang, Crystal Growth and the Magnetic Properties of  $\text{Na}_2\text{Co}_2\text{TeO}_6$  with Quasi-Two-Dimensional Honeycomb Lattice, *Cryst. Growth Des.* **19**, 2658 (2019).
  - <sup>14</sup> E. Lefrançois, M. Songvilay, J. Robert, G. Nataf, E. Jordan, L. Chaix, C. V. Colin, P. Lejay, A. Hadj-Azzem, R. Ballou, and V. Simonet, Magnetic properties of the honeycomb oxide  $\text{Na}_2\text{Co}_2\text{TeO}_6$ , *Phys. Rev. B* **94**, 214416 (2016).
  - <sup>15</sup> A. K. Bera, S. M. Yusuf, A. Kumar, and C. Ritter, Zigzag antiferromagnetic ground state with anisotropic correlation lengths in the quasi-two-dimensional honeycomb lattice compound  $\text{Na}_2\text{Co}_2\text{TeO}_6$ , *Phys. Rev. B* **95**, 094424 (2017).
  - <sup>16</sup> S. K. Pandey and J. Feng, Spin interaction and magnetism in cobaltate kitaev candidate materials: An ab initio and model hamiltonian approach, *Phys. Rev. B* **106**, 174411 (2022).
  - <sup>17</sup> W. Chen, X. Li, Z. Hu, Z. Hu, L. Yue, R. Sutarto, F. He, K. Iida, K. Kamazawa, W. Yu, X. Lin, and Y. Li, Spin-orbit phase behavior of  $\text{Na}_2\text{Co}_2\text{TeO}_6$  at low temperatures, *Phys. Rev. B* **103**, L180404 (2021).
  - <sup>18</sup> J. c. v. Chaloupka, G. Jackeli, and G. Khaliullin, Kitaev-Heisenberg Model on a Honeycomb Lattice: Possible Exotic Phases in Iridium Oxides  $\text{A}_2\text{IrO}_3$ , *Phys. Rev. Lett.*

- 105**, 027204 (2010).
- <sup>19</sup> Y. Singh, S. Manni, J. Reuther, T. Berlijn, R. Thomale, W. Ku, S. Trebst, and P. Gegenwart, Relevance of the Heisenberg-Kitaev Model for the Honeycomb Lattice Iridates  $A_2\text{IrO}_3$ , *Phys. Rev. Lett.* **108**, 127203 (2012).
- <sup>20</sup> Y. Singh and P. Gegenwart, Antiferromagnetic Mott insulating state in single crystals of the honeycomb lattice material  $\text{Na}_2\text{IrO}_3$ , *Phys. Rev. B* **82**, 064412 (2010).
- <sup>21</sup> S. K. Choi, R. Coldea, A. N. Kolmogorov, T. Lancaster, I. I. Mazin, S. J. Blundell, P. G. Radaelli, Y. Singh, P. Gegenwart, K. R. Choi, S.-W. Cheong, P. J. Baker, C. Stock, and J. Taylor, Spin Waves and Revised Crystal Structure of Honeycomb Iridate  $\text{Na}_2\text{IrO}_3$ , *Phys. Rev. Lett.* **108**, 127204 (2012).
- <sup>22</sup> A. Biffin, R. D. Johnson, S. Choi, F. Freund, S. Manni, A. Bombardi, P. Manuel, P. Gegenwart, and R. Coldea, Unconventional magnetic order on the hyperhoneycomb Kitaev lattice in  $\beta\text{-Li}_2\text{IrO}_3$ : Full solution via magnetic resonant x-ray diffraction, *Phys. Rev. B* **90**, 205116 (2014).
- <sup>23</sup> A. Biffin, R. D. Johnson, I. Kimchi, R. Morris, A. Bombardi, J. G. Analytis, A. Vishwanath, and R. Coldea, Non-coplanar and Counterrotating Incommensurate Magnetic Order Stabilized by Kitaev Interactions in  $\gamma\text{-Li}_2\text{IrO}_3$ , *Phys. Rev. Lett.* **113**, 197201 (2014).
- <sup>24</sup> B. H. Kim, G. Khaliullin, and B. I. Min, Electronic excitations in the edge-shared relativistic Mott insulator:  $\text{Na}_2\text{IrO}_3$ , *Phys. Rev. B* **89**, 081109 (2014).
- <sup>25</sup> H. Gretarsson, J. P. Clancy, X. Liu, J. P. Hill, E. Bozin, Y. Singh, S. Manni, P. Gegenwart, J. Kim, A. H. Said, D. Casa, T. Gog, M. H. Upton, H.-S. Kim, J. Yu, V. M. Katukuri, L. Hozoi, J. van den Brink, and Y.-J. Kim, Crystal-Field Splitting and Correlation Effect on the Electronic Structure of  $A_2\text{IrO}_3$ , *Phys. Rev. Lett.* **110**, 076402 (2013).
- <sup>26</sup> L. Clark and A. H. Abdeldaim, Quantum spin liquids from a materials perspective, *Annual Review of Materials Research* **51**, 495 (2021).
- <sup>27</sup> H. Takagi, T. Takayama, G. Jackeli, G. Khaliullin, and S. E. Nagler, Concept and realization of kitaev quantum spin liquids, *Nature Reviews Physics* **1**, 264 (2019).
- <sup>28</sup> S. M. Winter, Y. Li, H. O. Jeschke, and R. Valentí, Challenges in design of Kitaev materials: Magnetic interactions from competing energy scales, *Phys. Rev. B* **93**, 214431 (2016).
- <sup>29</sup> S.-H. Baek, S.-H. Do, K.-Y. Choi, Y. S. Kwon, A. U. B. Wolter, S. Nishimoto, J. van den Brink, and B. Büchner, Evidence for a field-induced quantum spin liquid in  $\alpha\text{-ruCl}_3$ , *Phys. Rev. Lett.* **119**, 037201 (2017).
- <sup>30</sup> J. S. Gordon, A. Catuneanu, E. S. Sørensen, and H.-Y. Kee, Theory of the field-revealed Kitaev spin liquid, *Nat. Commun.* **10**, 2470 (2019).
- <sup>31</sup> L. Janssen and M. Vojta, Heisenberg–kitaev physics in magnetic fields, *Journal of Physics: Condensed Matter* **31**, 423002 (2019).
- <sup>32</sup> B. Kim, P. Liu, J. M. Tomczak, and C. Franchini, Strain-induced tuning of the electronic coulomb interaction in  $3d$  transition metal oxide perovskites, *Phys. Rev. B* **98**, 075130 (2018).
- <sup>33</sup> K. Kataoka, D. Hirai, T. Yajima, D. Nishio-Hamane, R. Ishii, K.-Y. Choi, D. Wulferding, P. Lemmens, S. Kitakata, T. Sakakibara, et al., Kitaev spin liquid candidate  $\text{Os}_x\text{Cl}_3$  comprised of honeycomb nano-domains, *Journal of the Physical Society of Japan* **89**, 114709 (2020).
- <sup>34</sup> X.-L. Sheng and B. K. Nikolić, Monolayer of the  $5d$  transition metal trichloride  $\text{OsCl}_3$ : A playground for two-dimensional magnetism, room-temperature quantum anomalous hall effect, and topological phase transitions, *Phys. Rev. B* **95**, 201402 (2017).
- <sup>35</sup> J. G. Rau, E. K.-H. Lee, and H.-Y. Kee, Spin-orbit physics giving rise to novel phases in correlated systems: Iridates and related materials, *Annual Review of Condensed Matter Physics* **7**, 195 (2016).
- <sup>36</sup> S. K. Pandey, Q. Gu, Y. Lin, R. Tiwari, and J. Feng, Emergence of bond-dependent highly anisotropic magnetic interactions in  $\text{sr}_4\text{rho}_6$ : A theoretical study, *Phys. Rev. B* **107**, 115119 (2023).
- <sup>37</sup> P. H. Souza, D. P. d. A. Deus, W. H. Brito, and R. H. Miwa, Magnetic anisotropy energies and metal-insulator transitions in monolayers of  $\alpha\text{-RuCl}_3$  and  $\text{OsCl}_3$  on graphene, *Phys. Rev. B* **106**, 155118 (2022).
- <sup>38</sup> Q. Gu, S. K. Pandey, and Y. Lin, For crystal structure, methodology, phonon dispersion, magnetic anisotropy plot, validity of  $j_{\text{eff}} = 1/2$  picture and spin-wave spectra, refer to the supplemental material. (2023).
- <sup>39</sup> K. Hu, F. Wang, and J. Feng, First-principles study of the magnetic structure of  $\text{Na}_2\text{IrO}_3$ , *Phys. Rev. Lett.* **115**, 167204 (2015).
- <sup>40</sup> S. Hwan Chun, J.-W. Kim, J. Kim, H. Zheng, C. C. Stoumpos, C. Malliakas, J. Mitchell, K. Mehlawat, Y. Singh, Y. Choi, et al., Direct evidence for dominant bond-directional interactions in a honeycomb lattice iridate  $\text{Na}_2\text{IrO}_3$ , *Nat. Phys.* **11**, 462 (2015).
- <sup>41</sup> S. Middey, A. K. Nandy, S. Pandey, P. Mahadevan, and D. Sarma, Route to high néel temperatures in  $4d$  and  $5d$  transition metal oxides, *Phys. Rev. B* **86**, 104406 (2012).
- <sup>42</sup> S. K. Pandey, P. Mahadevan, and D. D. Sarma, Doping an antiferromagnetic insulator: A route to an antiferromagnetic metallic phase, *Europhysics Letters* **117**, 57003 (2017).
- <sup>43</sup> J. Reuther, R. Thomale, and S. Trebst, Finite-temperature phase diagram of the heisenberg-kitaev model, *Phys. Rev. B* **84**, 100406 (2011); R. Suttner, C. Platt, J. Reuther, and R. Thomale, Renormalization group analysis of competing quantum phases in the  $J_1\text{-}J_2$  heisenberg model on the kagome lattice, *Phys. Rev. B* **89**, 020408 (2014); M. Hering, F. Ferrari, A. Razpopov, I. I. Mazin, R. Valentí, H. O. Jeschke, and J. Reuther, Phase diagram of a distorted kagome antiferromagnet and application to  $\gamma\text{-kapellasite}$ , *npj Computational Materials* **8**, 10 (2022).
- <sup>44</sup> N. Astrakhantsev, F. Ferrari, N. Niggemann, T. Müller, A. Chauhan, A. Kshetrimayum, P. Ghosh, N. Regnault, R. Thomale, J. Reuther, T. Neupert, and Y. Iqbal, Pinwheel valence bond crystal ground state of the spin- $\frac{1}{2}$  heisenberg antiferromagnet on the shuriken lattice, *Phys. Rev. B* **104**, L220408 (2021); Y. Iqbal, H. O. Jeschke, J. Reuther, R. Valentí, I. I. Mazin, M. Greiter, and R. Thomale, Paramagnetism in the kagome compounds  $(\text{Zn,Mg,Cd})\text{Cu}_3(\text{OH})_6\text{Cl}_2$ , *Phys. Rev. B* **92**, 220404 (2015); Y. Watanabe, S. Trebst, and C. Hickey, Frustrated ferromagnetism of honeycomb cobaltates: Incommensurate spirals, quantum disordered phases, and out-of-plane ising order (2022), [arXiv:2212.14053 \[cond-mat.str-el\]](https://arxiv.org/abs/2212.14053).
- <sup>45</sup> G. Kresse and D. Joubert, From ultrasoft pseudopotentials to the projector augmented-wave method, *Phys. Rev. B* **59**, 1758 (1999).
- <sup>46</sup> P. E. Blöchl, Projector augmented-wave method, *Phys. Rev. B* **50**, 17953 (1994).

- <sup>47</sup> G. Kresse and J. Hafner, Ab initio molecular dynamics for liquid metals, *Phys. Rev. B* **47**, 558 (1993).
- <sup>48</sup> G. Kresse and J. Furthmüller, Efficiency of ab-initio total energy calculations for metals and semiconductors using a plane-wave basis set, *Comput. Mater. Sci.* **6**, 15 (1996).
- <sup>49</sup> G. Kresse and J. Furthmüller, Efficient iterative schemes for ab initio total-energy calculations using a plane-wave basis set, *Phys. Rev. B* **54**, 11169 (1996).
- <sup>50</sup> J. P. Perdew, K. Burke, and M. Ernzerhof, Generalized gradient approximation made simple, *Phys. Rev. Lett.* **77**, 3865 (1996).
- <sup>51</sup> S. L. Dudarev, G. A. Botton, S. Y. Savrasov, C. J. Humphreys, and A. P. Sutton, Electron-energy-loss spectra and the structural stability of nickel oxide: An LSDA+U study, *Phys. Rev. B* **57**, 1505 (1998).
- <sup>52</sup> A. Togo and I. Tanaka, First principles phonon calculations in materials science, *Scr. Mater.* **108**, 1 (2015).
- <sup>53</sup> A. Togo, First-principles phonon calculations with phonopy and phono3py, *J. Phys. Soc. Jpn.* **92**, 012001 (2023).
- <sup>54</sup> A. A. Mostofi, J. R. Yates, Y.-S. Lee, I. Souza, D. Vanderbilt, and N. Marzari, wannier90: A tool for obtaining maximally-localised Wannier functions, *Comput. Phys. Commun.* **178**, 685 (2008).
- <sup>55</sup> C. Franchini, R. Kovacik, M. Marsman, S. S. Murthy, J. He, C. Ederer, and G. Kresse, Maximally localized Wannier functions in  $\text{LaMnO}_3$  within PBE+U, hybrid functionals and partially self-consistent GW: an efficient route to construct *ab initio* tight-binding parameters for  $e_g$  perovskites, *Journal of Physics: Condensed Matter* **24**, 235602 (2012).
- <sup>56</sup> Q. Gu, S. K. Pandey, and R. Tiwari, A computational method to estimate spin-orbital interaction strength in solid state systems, *Comput. Mater. Sci.* **221**, 112090 (2023).
- <sup>57</sup> S. L. Adler, Quantum theory of the dielectric constant in real solids, *Phys. Rev.* **126**, 413 (1962).
- <sup>58</sup> N. Wiser, Dielectric constant with local field effects included, *Phys. Rev.* **129**, 62 (1963).
- <sup>59</sup> F. Aryasetiawan, M. Imada, A. Georges, G. Kotliar, S. Biermann, and A. I. Lichtenstein, Frequency-dependent local interactions and low-energy effective models from electronic structure calculations, *Phys. Rev. B* **70**, 195104 (2004).
- <sup>60</sup> F. L. Buessen, The SpinParser software for pseudofermion functional renormalization group calculations on quantum magnets, *SciPost Phys. Codebases*, 5 (2022).
- <sup>61</sup> J. Reuther and P. Wölfle,  $J_1-J_2$  frustrated two-dimensional heisenberg model: Random phase approximation and functional renormalization group, *Phys. Rev. B* **81**, 144410 (2010).
- <sup>62</sup> F. L. Buessen, V. Nocolak, S. Trebst, and J. Reuther, Functional renormalization group for frustrated magnets with nondiagonal spin interactions, *Phys. Rev. B* **100**, 125164 (2019).
- <sup>63</sup> S. Toth and B. Lake, Linear spin wave theory for single-q incommensurate magnetic structures, *J. Phys.: Condens. Matter* **27**, 166002 (2015).

## SUPPLEMENTARY MATERIALS

### 1. *Ab initio* calculations

#### a. Details of *ab initio* calculations

Density-functional theory (DFT) calculations have been performed using projector-augmented wave method<sup>45,46</sup>, implemented within Vienna *ab initio* simulation package (VASP)<sup>47-49</sup>. The Perdew-Burke-Ernzerhof functional<sup>50</sup> is used for the exchange-correlation functional within the GGA formalism. We start with the monoclinic ( $C2/m$ ) crystal structure for the monolayer  $\text{OsCl}_3$  with 2 Os atom unit cell as shown in Fig. S1(a). Full structural relaxation is performed on the  $2 \times 1 \times 1$  magnetic supercell with FM and ZZ magnetic orders (shown in Fig. S1(b)). The energy cutoff for a plane-wave basis is set to 500 eV and  $\Gamma$ -centered  $k$ -mesh of  $4 \times 8 \times 1$  is considered in our calculations. High accuracy of our calculations is ensured by tighter relaxation convergence criterion wherein tolerance considered for total energy is  $10^{-8}$  eV while for force it is  $5 \times 10^{-6}$  eV/Å. Full optimization of the crystal structure is performed after considering  $U = 1$  eV under Dudarev<sup>51</sup> scheme and spin-orbit coupling (SOC) effect at the self-consistent level. For both the cases of ZZ and FM states, optimization resulted in a similar crystal structure and optimized lattice constants are  $a = b = 6.1787$  Å, vacuum  $c = 25$  Å, and  $\alpha = \beta = 90^\circ$  and  $\gamma \approx 120^\circ$  and atomic coordinates of the final structure are listed in the Table S1. The primitive unit cell is shown in Fig. S1 (a) and the Brillouin zone (BZ) for the zigzag (ZZ) supercell is shown in Fig. S1 (c).

TABLE S1. Atomic coordinates in magnetic unit cell of monolayer  $\text{OsCl}_3$  with space group  $C2/m$ . Lattice constants are  $a = b = 6.1787$  Å,  $c = 25$  Å,  $\alpha = \beta = 90^\circ$  and  $\gamma = 119.88^\circ$

atom	$x/a$	$y/b$	$z/c$
Os1	0.166797	0.833203	0.500000
Os2	0.833203	0.166797	0.500000
Cl1	0.855480	0.855480	0.446984
Cl2	0.144520	0.144520	0.553016
Cl3	0.499663	0.143222	0.446932
Cl4	0.856778	0.500337	0.553068
Cl5	0.500337	0.856778	0.553068
Cl6	0.143222	0.499663	0.446932

#### b. Phonon dispersion

The pristine monolayer  $\text{OsCl}_3$  has not been observed experimentally yet. As explained in the main text, triangular lattice of  $\text{Os}^{+3}$  ions with nanometer-sized honeycomb domains is observed recently in experiments<sup>33</sup> This raises a natural question about the structural stability of the resulting monolayer honeycomb lattice. To answer

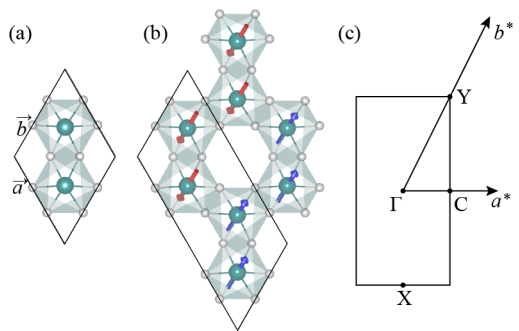


FIG. S1. (a) Primitive unit cell of  $\text{OsCl}_3$ , (b) the  $2 \times 1 \times 1$  supercell hosting ZZ magnetic order, and (c) BZ of the ZZ supercell.

this, we perform phonon calculations on a  $2 \times 4 \times 1$  supercell, while considering Hubbard  $U = 1$  eV on Os  $d$  orbitals and imposing ZZ magnetic configuration. We used the finite displacement method to calculate the force constants and phonon dispersions obtained with and without SOC effects are shown in Fig. S2. In both cases, crystal structure is at least dynamically stable as no soft modes are found in our calculations. The post-processing of these phonon calculations is done by Phonopy package<sup>52,53</sup>.

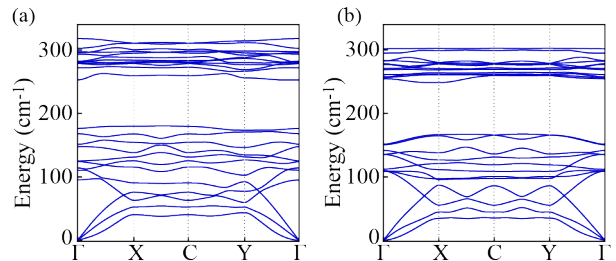


FIG. S2. Phonon dispersion plots for monolayer  $\text{OsCl}_3$  with ZZ magnetic order and  $U = 1$  eV on Os  $d$  orbitals calculated without (a) and with (b) SOC effect.

#### c. In-plane magnetic anisotropy

To obtain the magnetic anisotropy in monolayer  $\text{OsCl}_3$ , we start with magnetic moments aligned along  $\mathbf{a}$  axis in the FM state. We then rotate these moments by  $30^\circ$  in the  $\mathbf{ab}$  plane and perform total energy calculations. The upper limit of rotation was fixed at  $180^\circ$ . Obviously, at  $120^\circ$ , magnetic moments are aligned along the  $\mathbf{b}$  axis. The obtained plot is shown in Fig. S3. From this plot, one can conclude that while Os spins prefer to align along  $\mathbf{a}$  axis, the in-plane anisotropic energy is small in monolayer  $\text{OsCl}_3$ .



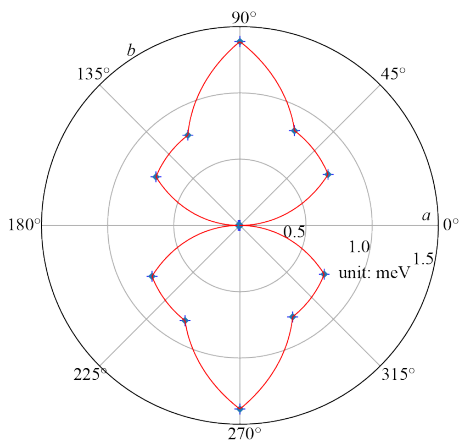


FIG. S3. In-plane magnetic anisotropy in monolayer  $\text{OsCl}_3$  estimated considering FM state. While Os spins prefer to align along  $\mathbf{a}$ , in-plane magnetic anisotropy is small in this material.

## 2. Estimation of electronic parameters

### a. Crystal field splitting and hopping amplitudes

Crystal field matrix and hopping amplitudes are estimated from a non-spin-polarised, SOC excluded tight-binding ( $H_{\text{TB}}$ ) Hamiltonian expressed in the local axes framework depicted in Fig. 1(a). These two terms can be given as,

$$H_{\text{TB}} = H_{\text{cf}} + H_{\text{hop}}$$

The above Hamiltonian can be obtained by projecting the *ab initio* band structure onto Wannier functions in which all the five Os- $d$  orbitals form the basis<sup>54,55</sup>. The choice of the local axes ( $\mathbf{x}$ ,  $\mathbf{y}$ ,  $\mathbf{z}$ ) in Fig. 1(a) along the oxygen atoms is such that  $\mathbf{c} = \mathbf{x} + \mathbf{y} + \mathbf{z}$  lies along trigonal distortion axis of the  $\text{OsCl}_6$  octahedra. Close agreement between the thus obtained TB model and *ab initio* band structure is shown in Fig. S4(a). Crystal field matrix on a site  $i$  ( $\Delta_i^{\text{CF}}$ ) in the above term  $H_{\text{cf}}$  is extracted from the onsite part of  $H_{\text{TB}}$  and is given by,

$$\Delta_i^{\text{CF}} = \begin{bmatrix} 2.6322 & -0.0772 & 0.2578 & -0.0122 & 0.0369 \\ -0.0772 & 0.0479 & -0.0268 & 0.0709 & 0.0272 \\ 0.2578 & -0.0268 & 0.0707 & 0.1026 & 0.0366 \\ -0.0122 & 0.0709 & 0.1026 & 2.6244 & 0.2800 \\ 0.0369 & 0.0272 & 0.0366 & 0.2800 & 0.0748 \end{bmatrix} \quad (\text{S1})$$

Entries in the above matrix are in eV. Hopping amplitudes up to third neighbor are listed below in Table S2.

### b. Estimation of SOC strength ( $\lambda$ )

To extract SOC strength in  $\text{OsCl}_3$ , we added an onsite SOC term to the TB Hamiltonian as<sup>56</sup>,

$$H = \mathcal{I}_2 \otimes H_{\text{TB}} + H_{\text{soc}}$$

where  $\mathcal{I}_2$  is the two-dimensional identity matrix and  $\otimes$  is the Kronecker product.  $H_{\text{soc}} = \sum_i \lambda \mathbf{L}_i \cdot \mathbf{s}_i$  is the onsite SOC interaction term that couples the electronic spin ( $\mathbf{S}$ ) and its orbital momentum ( $\mathbf{L}$ ) with a strength  $\lambda$ . Here, the SOC strength  $\lambda$  is estimated by fitting the eigenvalues of  $H$  with those obtained from SOC included *ab initio* band structure calculations as the target. The best agreement between these two band structures, shown in Fig. S4(b), is obtained for  $\lambda = 0.335$  eV which is considered in further calculations.

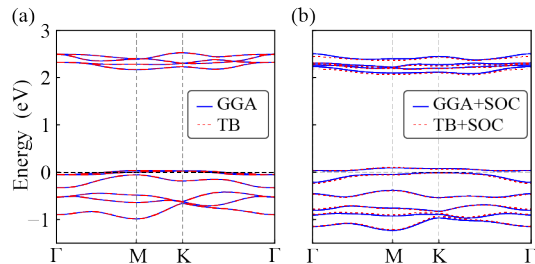


FIG. S4. Comparison of *ab initio* and TB model band structures for, (a) non-spin-polarized case, and (b) SOC included case. In (b), SOC effects in *ab initio* calculations are included self-consistently, which then fitted with the TB Hamiltonian obtained in (a) after explicitly adding onsite SOC term  $H_{\text{soc}} = \sum_i \lambda \mathbf{L}_i \cdot \mathbf{s}_i$  to  $H_{\text{TB}}$ .

### c. Estimation of Hubbard $U$ and Hund's $J_H$ within cRPA

We estimate the Coulomb matrix elements  $U_{ijkl}(\omega = 0)$  within the constrained random phase approximation (cRPA) implemented with VASP<sup>57-59</sup>. We neglect the screening effects for all the five Os  $d$  orbital states which are energetically well-separated from other states (see Fig. S4). The estimated parameters are  $U = 3.8$  eV and  $J_H = 0.143$  eV.

## 3. Validity of $j_{\text{eff}} = 1/2$ picture

It is crucial to analyze the effects of various electronic interactions on the band structure of monolayer  $\text{OsCl}_3$ . Such analysis can help us to examine the validity of low-energy  $j_{\text{eff}} = 1/2$  picture, which is considered a building block for the emergence of dominant Kitaev interaction. To this end, *ab initio* band structure calculations are performed for three cases, *viz* SOC, SOC +  $U$ , and SOC +  $U$  + ZZ magnetic state. Obtained results are then projected onto  $j_{\text{eff}} = 1/2$  and  $3/2$  states, eigenfunctions of which are given below in Eq. S2.

TABLE S2. First, second and third neighbor Os-Os hopping amplitudes (in eV) on different types of bonds listed in the basis  $\psi^\dagger = [d_{z^2}^\dagger, d_{xz}^\dagger, d_{yz}^\dagger, d_{x^2-y^2}^\dagger, d_{xy}^\dagger]$

X <sub>1</sub> -bond					Y <sub>1</sub> -bond					Z <sub>1</sub> -bond				
$\begin{pmatrix} -0.0183 & -0.0150 & -0.1032 & 0.0291 & -0.0521 \\ -0.0150 & 0.0653 & -0.0670 & -0.0074 & 0.1817 \\ -0.1032 & -0.0670 & -0.0762 & 0.1708 & 0.0028 \\ 0.0291 & -0.0074 & 0.1708 & 0.0097 & 0.0405 \\ -0.0521 & 0.1817 & 0.0028 & 0.0405 & 0.0151 \end{pmatrix}$	$\begin{pmatrix} 0.0323 & -0.0899 & -0.0070 & 0.0027 & 0.0193 \\ -0.0899 & -0.0784 & 0.0121 & -0.1796 & -0.0473 \\ -0.0070 & 0.0121 & 0.0100 & -0.0476 & 0.1845 \\ 0.0027 & -0.1796 & -0.0476 & -0.0431 & -0.0016 \\ 0.0193 & -0.0473 & 0.1845 & -0.0016 & 0.0742 \end{pmatrix}$	$\begin{pmatrix} -0.0265 & 0.0477 & -0.0163 & -0.0228 & 0.2041 \\ 0.0477 & 0.0212 & 0.1853 & 0.0196 & 0.0170 \\ -0.0163 & 0.1853 & 0.0650 & 0.0179 & -0.0533 \\ -0.0228 & 0.0196 & 0.0179 & 0.0141 & 0.0077 \\ 0.2041 & 0.0170 & -0.0533 & 0.0077 & -0.0782 \end{pmatrix}$												
X <sub>2</sub> -bond					Y <sub>2</sub> -bond					Z <sub>2</sub> -bond				
$\begin{pmatrix} -0.0213 & 0.0404 & -0.0290 & 0.0126 & -0.0045 \\ 0.0500 & 0.0033 & -0.0083 & -0.0206 & -0.0514 \\ -0.0590 & -0.0213 & 0.0000 & 0.0746 & 0.0163 \\ 0.0006 & -0.0201 & 0.0977 & 0.0323 & -0.0414 \\ -0.0125 & -0.0479 & 0.0077 & -0.0362 & -0.0100 \end{pmatrix}$	$\begin{pmatrix} 0.0230 & -0.0353 & 0.0376 & 0.0151 & -0.0054 \\ -0.0712 & -0.0011 & 0.0109 & -0.0742 & -0.0063 \\ 0.0384 & 0.0196 & -0.0104 & 0.0145 & -0.0531 \\ 0.0279 & -0.0885 & 0.0043 & -0.0107 & 0.0570 \\ -0.0010 & -0.0181 & -0.0486 & 0.0486 & -0.0034 \end{pmatrix}$	$\begin{pmatrix} 0.0181 & -0.0222 & -0.0433 & -0.0306 & 0.0921 \\ -0.0316 & -0.0155 & -0.0534 & 0.0241 & 0.0186 \\ -0.0386 & -0.0491 & 0.0015 & -0.0277 & -0.0185 \\ -0.0189 & 0.0285 & -0.0363 & 0.0006 & 0.0140 \\ 0.0979 & 0.0110 & -0.0065 & -0.0239 & -0.0004 \end{pmatrix}$												
X <sub>3</sub> -bond					Y <sub>3</sub> -bond					Z <sub>3</sub> -bond				
$\begin{pmatrix} 0.0239 & 0.0031 & -0.0241 & 0.0315 & 0.0131 \\ 0.0031 & 0.0086 & 0.0073 & -0.0044 & -0.0108 \\ -0.0241 & 0.0073 & -0.0289 & 0.0149 & 0.0038 \\ 0.0315 & -0.0040 & 0.0149 & -0.0039 & -0.0062 \\ 0.0131 & -0.0108 & 0.0038 & -0.0062 & 0.0103 \end{pmatrix}$	$\begin{pmatrix} 0.0304 & 0.0003 & -0.0019 & -0.0269 & 0.0035 \\ 0.0003 & -0.0285 & 0.0049 & -0.0284 & 0.0090 \\ -0.0019 & 0.0049 & 0.0104 & 0.0155 & -0.0120 \\ -0.0269 & -0.0288 & 0.0155 & -0.0105 & 0.0066 \\ 0.0035 & 0.0090 & -0.0120 & 0.0066 & 0.0073 \end{pmatrix}$	$\begin{pmatrix} -0.0230 & -0.0140 & -0.0071 & -0.0032 & 0.0241 \\ -0.0140 & 0.0092 & -0.0116 & -0.0095 & 0.0054 \\ -0.0071 & -0.0116 & 0.0081 & -0.0009 & 0.0089 \\ -0.0032 & -0.0095 & -0.0009 & 0.0448 & 0.0010 \\ 0.0241 & 0.0054 & 0.0089 & 0.0100 & -0.0292 \end{pmatrix}$												

$$\begin{aligned}
\left| \frac{1}{2}, \pm \frac{1}{2} \right\rangle &= \frac{1}{\sqrt{3}} \left( \mp |d_{xy}; \pm \frac{1}{2}\rangle \mp i |d_{xz}; \mp \frac{1}{2}\rangle - |d_{yz}; \mp \frac{1}{2}\rangle \right) \\
\left| \frac{3}{2}, \pm \frac{3}{2} \right\rangle &= \frac{1}{\sqrt{2}} \left( -i |d_{xz}; \pm \frac{1}{2}\rangle \mp |d_{yz}; \pm \frac{1}{2}\rangle \right) \\
\left| \frac{3}{2}, \pm \frac{1}{2} \right\rangle &= \frac{1}{\sqrt{6}} \left( 2 |d_{xy}; \pm \frac{1}{2}\rangle - i |d_{xz}; \mp \frac{1}{2}\rangle \mp |d_{yz}; \mp \frac{1}{2}\rangle \right)
\end{aligned} \tag{S2}$$

Plots obtained for the three cases are shown in Fig. S5(a), (b) and (c) respectively. SOC effect is included at the self-consistent level in all these calculations.

Certain features of the band structures can immediately be identified. Firstly, one can find a clear separation between narrow  $j_{\text{eff}} = 1/2$  and  $3/2$  bands for SOC-only band structure shown in Fig. S5(a). In Fig. S5(b), for the SOC + U case, the  $j_{\text{eff}} = 1/2$  bands near the Fermi level remain largely unaffected at this  $U = 1$  eV (though a larger  $U = 2$  eV opens a clear band gap which is not shown here) and the system is nearly insulating in both cases. This differs from the  $\alpha$ -RuCl<sub>3</sub> picture presented by Kim *et. al.*<sup>6</sup> where  $U = 1.5$  eV was necessary to bring out a clear  $j_{\text{eff}} = 1/2$ - $3/2$  separation and to drive the system insulating. The weak response towards smaller  $U$  along with the narrow bandwidth ( $\sim 0.3$  eV) of  $j_{\text{eff}} = 1/2$  states may be hinting that  $t$  and  $U$  parameters have similar scales in this material. A constrained random phase approximation (cRPA) estimation brings  $U = 3.8$  eV and  $J_{\text{H}} = 0.143$  eV for monolayer OsCl<sub>3</sub>. However, the largest 1NN hopping magnitude  $|t|$  estimated from the Wannier TB model is  $\approx 0.2$  eV. Based on these values, one can still think of limit  $t \ll U$  and hence the formation of well-localized  $j_{\text{eff}}$  states in this compound. A wider band gap opens up once magnetism in the form of ZZ state is included and obtained band structure for this case is shown in Fig. S5(c).

#### 4. Second-order perturbation method

The full Hamiltonian for the  $d^5$  Os<sup>+3</sup> ions is given by,

$$\mathcal{H} = H_{\text{hop}} + H_{\text{cf}} + H_{\text{soc}} + H_{\text{int}} \tag{S3}$$

where the terms on the right-hand side are hopping, CF, SOC, and Hubbard-Kanamori interaction Hamiltonians. Using the basis  $\psi_{i\sigma}^\dagger = [d_{z^2}^\dagger, d_{xz}^\dagger, d_{yz}^\dagger, d_{x^2-y^2}^\dagger, d_{xy}^\dagger]_{i\sigma}$  at site  $i$  of Os and spin  $\sigma$ , above Hamiltonian then reads,

$$\begin{aligned}
\mathcal{H} &= \sum_{i \neq j, \sigma} \psi_{i\sigma}^\dagger T_{ij} \psi_{j\sigma} + \sum_{i, \sigma} \psi_{i\sigma}^\dagger \Delta_i^{\text{CF}} \psi_{i\sigma} + \sum_i \lambda \mathbf{L}_i \cdot \mathbf{s}_i \\
&+ \frac{U}{2} \sum_{i, \alpha} n_{i\alpha\sigma} n_{i\alpha\sigma'} + \frac{U'}{2} \sum_{i, \alpha \neq \beta} n_{i\alpha} n_{i\beta} \\
&- \frac{J_{\text{H}}}{2} \sum_{i, \sigma, \sigma', \alpha \neq \beta} \psi_{i\alpha\sigma}^\dagger \psi_{i\alpha\sigma'} \psi_{i\beta\sigma'}^\dagger \psi_{i\beta\sigma} \\
&- \frac{J'}{2} \sum_{i, \sigma \neq \sigma', \alpha \neq \beta} \psi_{i\alpha\sigma}^\dagger \psi_{i\beta\sigma'} \psi_{i\alpha\sigma'}^\dagger \psi_{i\beta\sigma}
\end{aligned} \tag{S4}$$

In the above expression, the first three terms are hoppings, CF and SOC, while the last four terms are the Hubbard-Kanamori interactions. The  $U/U'$  are intra-orbital/interorbital Hartree energies and  $J_{\text{H}}$  and  $J'$  are Hund's coupling and pair hopping interaction, respectively. Rotational invariance in the isolated atom limit dictates the relationships:  $U' = U - 2J_{\text{H}}$  and  $J_{\text{H}} = J'$ . Hopping amplitudes  $T_{ij}$  and CF matrix  $\Delta_i^{\text{CF}}$  can be obtained by fitting the *ab initio* band structure with a TB model as described earlier.

In the limit  $t \ll U$ , i.e. in the isolated atom limit, one can separate the ‘‘onsite’’ term  $H_i^0$  at a site  $i$  from  $\mathcal{H}$  as,

$$H_i^0 = H_{\text{cf}} + H_{\text{soc}} + H_{\text{int}}$$

We drop index  $i$  since this Hamiltonian is the same for each site. The key here is that the  $d^5$  manifold has a two-fold degenerate ground state, which forms a pseudospin doublet and can be treated as a pseudospin-1/2. In order to extract the magnetic interactions of these pseudospin states, we first project the full TB Hamiltonian onto the pseudospin  $j_{1/2}$  space  $\{|\phi_{i\alpha}\rangle\}$ ,  $\alpha = \uparrow, \downarrow$ , where  $\uparrow, \downarrow$  refer to the SOC pseudospin-1/2 states. Starting from the isolated limit we introduce  $H_{\text{hop}}$  as a perturbation. In the second-order perturbation theory, the Hamiltonian is written as,

$$H^{(2)} = \sum_{ij} \sum_{\alpha\beta\alpha'\beta'} \mathcal{H}(i, j)_{\alpha\beta\alpha'\beta'} |\alpha, j\rangle \langle \alpha', j\rangle,$$

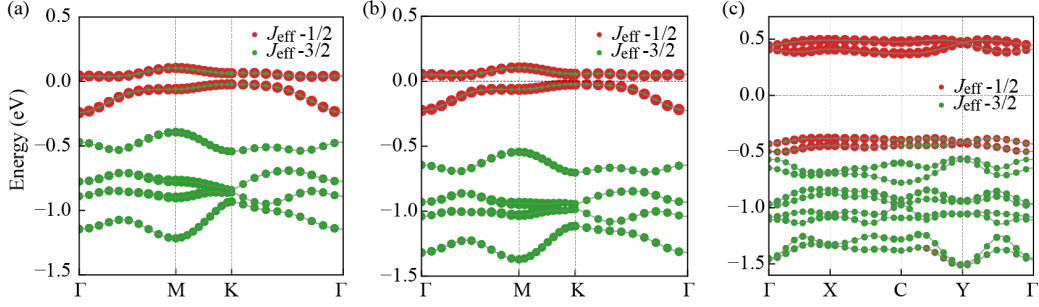


FIG. S5. Band structure plots of monolayer  $\text{OsCl}_3$  for, (a) SOC included, (b) SOC +  $U$ , and (c) SOC +  $U$  + ZZ magnetic state are shown. Red and green spheres depicted the weight of  $j_{\text{eff}} = 1/2$  and  $3/2$  states, respectively. Fermi energy is set to zero in these plots.

$$\mathcal{H}(i, j)_{\alpha\beta\alpha'\beta'} = \sum_{kl} \sum_{\gamma\lambda} \frac{1}{\Delta E} \langle i\alpha, j\beta | H_{\text{hop}} | k\gamma, l\lambda \rangle \times \langle k\gamma, l\lambda | H_{\text{hop}} | i\alpha', j\beta' \rangle, \quad (\text{S5})$$

where  $1/\Delta E = \frac{1}{2}[1/(E_{i\alpha} + E_{j\beta} - E_{k\lambda} - E_{l\gamma}) + 1/(E_{i\alpha'} + E_{j\beta'} - E_{k\lambda} - E_{l\gamma})]$ . Here,  $|i\alpha, j\beta\rangle$  and  $|i\alpha', j\beta'\rangle$  are two-site states in the  $j_{\text{eff}} = 1/2$  ground states, and  $|k\lambda, l\gamma\rangle$  are two-site excited states, both in the isolated atom limit.  $H_{\text{hop}}$  connects a two-site ground state to an excited state with  $(d^4, d^6)$  configuration, the dimensions of whose Hilbert spaces is 210. The eigenstates of isolated Os with 4, 5, and 6  $d$  electrons are obtained by exact diagonalization. One can represent the pseudo-spins  $j_{1/2}$  as  $S^\mu = \langle i\alpha | \mathbf{j}_{i, \text{eff}}^\mu | i\beta \rangle$  which are the expectation values of pseudospin  $\mathbf{j}_{\text{eff}}^\mu$  operators with  $\mu = 0, x, y, z$ . Here,  $\mathbf{j}_{\text{eff}}^0 = \mathcal{I}_2$  is the matrix representation of operator  $\mathbf{j}_{\text{eff}}^0$ . Eq. (S5) can be mapped to a spin Hamiltonian of the form,

$$H_{\text{spin}} = S_i^\mu \eta(i, j)^{\mu\nu} S_j^\nu = \frac{1}{4} \eta(i, j)^{\mu\nu} \phi_{i\alpha}^\dagger \sigma_{\alpha\alpha'}^\mu \phi_{i\alpha'} \phi_{j\beta} \sigma_{\beta\beta'}^\nu \phi_{j\beta}^\dagger, \quad (\text{S6})$$

where  $\mu, \nu = 0, x, y, z$ ,  $\sigma^\mu$  are Pauli matrices, and summation over all repeated indexes is implied. The map can be achieved by solving the linear equations

$$-\frac{1}{4} \sigma_{\alpha\alpha'}^\mu \sigma_{\beta\beta'}^\nu \eta(ij)^{\mu\nu} = \mathcal{H}(i, j)_{\alpha\beta\alpha'\beta'} \quad (\text{S7})$$

Thus, the most general form of exchange interaction matrix on the three Os-Os bonds can be written as,

$$\begin{aligned} \eta_X &= \begin{pmatrix} J + K & \Gamma' + \zeta & \Gamma' - \zeta \\ \Gamma' + \zeta & J + \xi & \Gamma \\ \Gamma' - \zeta & \Gamma & J - \xi \end{pmatrix} \\ \eta_Y &= \begin{pmatrix} J + \xi & \Gamma' + \zeta & \Gamma \\ \Gamma' + \zeta & J + K & \Gamma' - \zeta \\ \Gamma & \Gamma' - \zeta & J - \xi \end{pmatrix} \\ \eta_Z &= \begin{pmatrix} J + \xi & \Gamma & \Gamma' + \zeta \\ \Gamma & J - \xi & \Gamma' - \zeta \\ \Gamma' + \zeta & \Gamma' - \zeta & J + K \end{pmatrix} \end{aligned} \quad (\text{S8})$$

Only these symmetric components of interaction matrices appear on the first and third neighbor bonds, while on the second neighbor bonds, due to the absence of inversion symmetry, an additional antisymmetric component appears in the form of Dzyaloshinskii–Moriya interaction (DMI). The matrix from these antisymmetric interactions is given in Ref.<sup>28</sup>.

#### a. Three and four orbital terms

Since we consider both  $t_{2g}$  and  $e_g$  orbitals in our basis above, to ensure the rotational invariance of the “on-site” Hamiltonian  $H_i^0$ , one should include three and four orbital terms in the Hubbard-Kanamori Hamiltonian. Three orbital terms can be given,

$$\begin{aligned} H_{\text{int}}^{3\text{orb}} &= \frac{V_1}{2} \sum_{\sigma, \sigma', \alpha \neq \beta} \psi_{i\alpha\sigma}^\dagger \psi_{i\beta\sigma} \psi_{i\gamma\sigma'}^\dagger \psi_{i\gamma\sigma'} \\ &+ \frac{V_1}{2} \sum_{\sigma, \sigma', \alpha \neq \beta} \psi_{i\alpha\sigma}^\dagger \psi_{i\gamma\sigma} \psi_{i\gamma\sigma'}^\dagger \psi_{i\beta\sigma'} \\ &+ \frac{V_2}{2} \sum_{\sigma \neq \sigma', \alpha \neq \beta} \psi_{i\alpha\sigma}^\dagger \psi_{i\gamma\sigma} \psi_{i\beta\sigma'}^\dagger \psi_{i\gamma\sigma'} \\ &+ \frac{V_2}{2} \sum_{\sigma \neq \sigma', \alpha \neq \beta} \psi_{i\gamma\sigma}^\dagger \psi_{i\alpha\sigma} \psi_{i\gamma\sigma'}^\dagger \psi_{i\beta\sigma'} \end{aligned} \quad (\text{S9})$$

In the above equation, indices  $\alpha, \beta = d_{z^2}/d_{x^2-y^2}$  and  $\gamma = d_{xz}/d_{yz}$ . Magnitude of  $V_1, V_2$  are usually quite small ( $< 10^{-2}$  eV). Four orbital terms in the Hubbard-Kanamori Hamiltonian can be given as,

$$H_{\text{int}}^{4\text{orb}} = \frac{V}{2} \sum_{\sigma, \sigma', \alpha \neq \beta} \psi_{i\alpha\sigma}^\dagger \psi_{i\delta\sigma} \psi_{i\beta\sigma'}^\dagger \psi_{i\gamma\sigma'} \quad (\text{S10})$$

In the above equation, the four distinct orbital indices  $\alpha, \beta, \gamma$ , and  $\delta$  run over all the five  $d$  orbitals in our basis. The magnitude of  $V$  is usually of the order of  $\sim 10^{-3}$  eV. Addition of  $H_{\text{int}}^{3\text{orb}}$  and  $H_{\text{int}}^{4\text{orb}}$  to  $H_{\text{int}}$  term of Eq. 2 in the main text modify the magnetic interactions mostly at the third decimal places. This is consistent with the fact that these additional terms are redundant in the presence of large crystal field splitting ( $\Delta_i^{\text{CF}}$  in Eq. S1) which is also the case of monolayer  $\text{OsCl}_3$ . Since these significantly

smaller changes in magnetic interactions do not bring any substantial changes in the magnetic ground state, we used only two orbital terms of Eq. 2 for the phase diagram in Fig. 2(a) of the main text.

### 5. Pseudo-fermion functional renormalization group calculations

We use SpinParser package<sup>60</sup> to perform pseudo-fermion functional renormalization group (pf-FRG) calculations<sup>61,62</sup> on generalized Kitaev spin model obtained in the previous section. We consider honeycomb lattice to initialize vertex functions in order to capture two-particle interactions on lattice sites separated by up to 7 lattice bonds. In pf-FRG calculations, the single-particle vertex  $\Sigma^\Lambda(\omega)$  and two-particle vertex basis functions  $\Gamma^\Lambda(\omega, \omega', \omega'')$  are parameterized by a frequencies  $\omega$  and the renormalization group cutoff  $\Lambda$ . Here, then we use a logarithmically spaced mesh of discrete frequencies as

$$\omega_n = \omega_{\min} \left( \frac{\omega_{\max}}{\omega_{\min}} \right)^{\frac{n}{N_\omega - 1}}; \quad n = (0, 1, \dots, N_\omega - 1).$$

where  $\omega_{\min}$  and  $\omega_{\max}$  are the limit points of frequency on the positive half-axis which are set to be 0.01 and 35.0 respectively.  $N_\omega$  is the overall number of positive frequencies and is chosen to be 32 in our case. As for the negative half-axis, the frequencies are generated automatically by symmetry. The discretization of the cutoff parameter  $\Lambda$  is also done on a logarithmically spaced mesh given by,

$$\Lambda_n = \Lambda_{\max} b^n; \quad n = 0, \dots, \left\lfloor \log_b \left( \frac{\Lambda_{\min}}{\Lambda_{\max}} \right) \right\rfloor$$

where the  $\Lambda_{\min}$  and  $\Lambda_{\max}$  are the lower and upper boundaries of  $\Lambda$  which are set to be 0.01 and 50, respectively. The parameter  $b$  is step size and is set to be 0.98 in our calculations. Though we have considered up to 3NN interactions in our pf-FRG calculations, negligibly small 2NN and 3NN magnetic interactions do not affect the magnetic ground state obtained with this method at a qualitative level. We find that most part of the phase points in Fig. 2(a) of the main text can be described by dominant 1NN magnetic interactions only.

### 6. Atomic features

One of the quantities which can be measured from the resonant inelastic X-ray scattering (RIXS) experiments are single-point excitations represented by sharp peaks in the scattering intensity in the relevant energy range. It can be a direct probe for cubic symmetry lowering of the Rh-O<sub>6</sub> octahedra in a material. Theoretically, such a low-lying crystal field-assisted many-body excitations bear a close resemblance with the eigenvalues obtained

from diagonalization of many-body ‘‘onsite’’ Hamiltonian  $H^0$ . Hence, we discuss here the nature of CF splitting in monolayer OsCl<sub>3</sub> and its effect on the electronic structure. The CF matrix is given in Eq. S1.

Examining eigenvalues of CF matrix ( $\Delta_i$ ) in Eq. S1 reveals that  $t_{2g-e_g} \Delta_i^{t_{2g}-e_g} \approx 2.60$  eV and there is additional trigonal distortion  $\Delta_i^{\text{tri}} \approx 64$  meV of the octahedra. Eigenvalues obtained after exact diagonalization of  $H_i^0$  with this  $\Delta_i^{\text{CF}}$  can be compared with the single-point excitations observed in RIXS experiments. In our calculation, we find  $j_{\text{eff}}=1/2 - 3/2$  separation to be 0.580 eV which is approximately  $\frac{3}{2}\lambda$  for  $\lambda = 0.355$  eV estimated from band structure fitting of monolayer OsCl<sub>3</sub>. The four-fold  $j_{\text{eff}}=3/2$  states are split into two doublets which are separated by  $\approx 56$  meV. This splitting is a direct consequence of  $\Delta_i^{\text{tri}}$  present and is also found in Iridates and  $\alpha$ -RuCl<sub>3</sub>. By putting  $\Delta_i^{\text{tri}} = 0$  eV, as expected,  $j_{\text{eff}}=3/2$  states regained the four-fold degeneracy.

### 7. Magnetic interaction and ground state from cRPA parameters

Below in Table S3, we provide estimated magnetic interactions corresponding to parameters obtained from cRPA, i.e.  $U = 3.8$  eV and  $J_{\text{H}} = 0.143$  eV.

TABLE S3. Estimated bond-dependent magnetic interactions for cRPA estimated  $U = 3.8$  eV,  $J_{\text{H}} = 0.143$  eV. Here also,  $\lambda = 0.355$  eV. Values of Heisenberg  $J$ , Kitaev  $K$ , off-diagonal  $\Gamma$ , and  $\Gamma'$  terms along with diagonal and off-diagonal anisotropic terms  $\xi$  and  $\zeta$  are listed. 3NN interactions as well as some 2NN interactions are  $< 0.05$  meV and hence not listed here.

Bond	Magnetic interactions (meV)					
	$J$	$K$	$\Gamma$	$\Gamma'$	$\xi$	$\zeta$
X <sub>1</sub>	0.057	-1.318	0.428	-0.334	-	0.235
Y <sub>1</sub>	0.068	-1.571	0.465	-0.051	-	-0.364
Z <sub>1</sub>	0.043	-1.396	0.372	-0.212	-	-0.388
X <sub>2</sub>	-	0.075	-	-	-	-
Y <sub>2</sub>	0.132	0.126	-	-	-	-
Z <sub>2</sub>	-	0.068	-	-	-	-
$D_{ij}$						
X <sub>2</sub>						
Y <sub>2</sub>	$<  0.04 $					
Z <sub>2</sub>						

We use these interactions from Table S3 in the pf-FRG calculations and the static spin correlation for the corresponding ZZ ground state is shown in Fig. S6. One of the  $M$  points of the first BZ contributes to this ground state indicating some sort of ‘‘anisotropic’’ ZZ state.



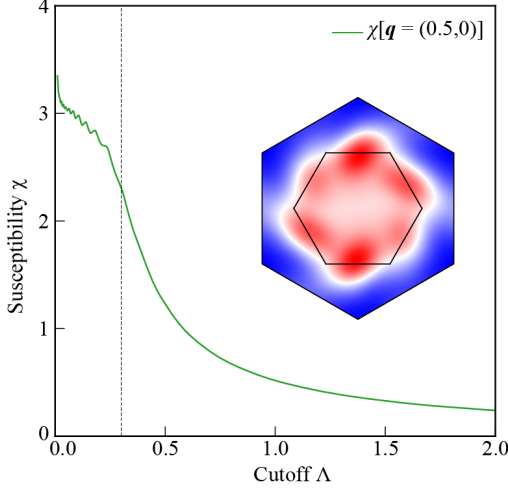


FIG. S6. Static spin correlations plot, shown in the inset, obtained from pf-FRG calculations using magnetic interactions from Table S3. Intensity contribution from one of the  $M$  points of the BZ indicates a ZZ ground state. The renormalization group flow of the magnetic correlation ( $\chi$ ) represented by the green curve breaks at  $\approx 0.3 \Lambda$  indicating the onset of the long-range magnetic order.

### 8. Quantitatively different zigzag states in phase diagram

As we have mentioned that different part of the phase diagram in Fig. 2(a) of the main text hosts different magnetic ground state depending upon the nature of dominant magnetic interactions. The largest part of the phase diagram is occupied by the ZZ magnetic state which differs quantitatively in different regions of the phase space. To demonstrate this point, we plot two of them in Fig. S7. Spin orientations in these two ZZ states are obtained by optimization of classical ground state using SpinW package<sup>63</sup>. As one can see in Fig. S7(a), spin alignment is in-plane while spins are tilted in the out-of-plane direction in Fig. S7(b). In-plane configuration corresponds to  $J = 0.4$  meV and  $K = -18.2$  meV and out-of-plane config-

uration is obtained from interactions listed in Table S3. Corresponding spin-wave spectrum, calculated using linear spin-wave theory as implemented in SpinW<sup>63</sup>, are also shown in Fig. S7(c) and (d).

As one can see that the spectra are gapless in Fig. S7(c) for the in-plane alignment of spins and are gapped in Fig. S7(d) for the out-of-plane tilting of spins. This distinctive feature of the spectra can be understood as follows. In the absence of magnetic couplings like  $\Gamma$  and  $\Gamma'$ , any in-plane spin alignment would classically have the same energy resulting in a gapless mode. This can be seen for the spin alignment of Fig. S7(a) results in a gapless mode at  $Y$  point. However,  $\Gamma$  and  $\Gamma'$  terms dictate the out-of-plane tilting of spins and pinning down of moments in a specific direction (along one of the Cl-Cl edges in Os-Cl $_{\alpha}$  octahedra, see Fig. 1 (a)). This intro-

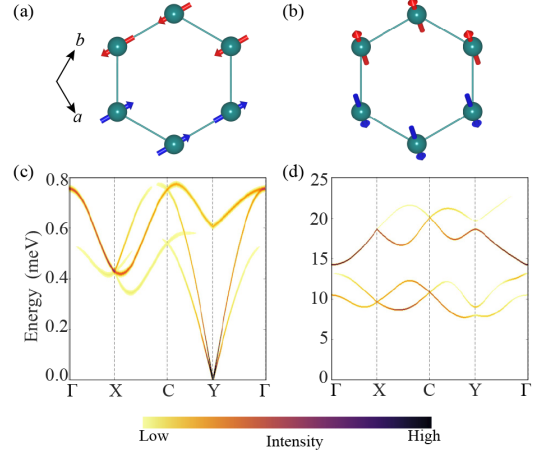


FIG. S7. Optimized classical magnetic ground states for interactions corresponding to, (a)  $J = 0.4$  meV and  $K = -18.2$  meV, and (b) interaction listed in Table S3. Spin wave spectra obtained using linear spin wave theory for, (c) in-plane configuration shown in (a), and (d) out-of-plane shown in (b)

duces additional anisotropy in the Hamiltonian causes the spectra to be gapped. Diagonal anisotropic term  $\xi$  may lead to further anisotropy in the system, in-turn actively contributing to gapped spectra.